Journal of Electroanalytical Chemistry 1001 (2026) 119653

Contents lists available at ScienceDirect

Journal of Electroanalytical Chemistry

journal homepage: www.elsevier.com/locate/jelechem

Architecture-driven design of ZnO@C anodes in next-generation zinc-based batteries: Toward practical energy storage systems

Elisa Emanuele [a,*], Lucia Mancini [b], Seyedamin Razaghi [a], Rožle Repič [b], Maya Kobchenko [b], Benedetto Bozzini [a]

[a] Department of Energy, Politecnico di Milano, via Lambuschini 4, 20156 Milano, Italy
[b] Slovenian National Building and Civil Engineering Institute (ZAG), Dimičeva ulica 12, SI-1000 Ljubljana, Slovenia

ARTICLE INFO

Keywords:
Zn anode
Zinc-alkaline batteries
Nanostructured electrodes
Electrode architecture
ZnO nanoparticle
X-ray microtomography

ABSTRACT

Zinc-based batteries are promising for sustainable energy storage due to their low cost and environmental friendliness. However, challenges such as passivation, low cycle life, and limited zinc utilization hinder practical commercialization. In this study, we address these challenges using ZnO@C nanoparticles (NPs) as anode active material, optimizing slurry formulation and electrode architectures. PTFE and CMC were employed as complementary binders to enhance mechanical integrity, wettability, and zinc utilization, while reducing the reliance on fluorinated binders. Two electrode fabrication methods — blade coating and hot pressing — were evaluated to assess the effects of active layer thickness on performance and durability. Full-cell Zn/Ni tests were run under harsh testing condition: closed cell, low amount of electrolyte and no additive or ZnO saturation. We found that thinner (ca. 100 μm), blade-coated ZnO@C anodes outperformed thicker (ca. 400 μm) hot-pressed electrodes in both cycle life and specific capacity. Blade-coated electrodes maintained a discharge-specific capacity exceeding 400 mAh g^{-1} for over 200 cycles and achieved a maximum of 524 mAh g^{-1}, approximately 80 % of ZnO theoretical capacity. Post-mortem X-ray computed microtomography analyses revealed that the crucial electrode architecture parameters are ZnO particle accessibility and even utilization in the electrode bulk. These resulted to be optimal in blade-coated electrodes, while heterogeneities and untransformed ZnO volumes were found in the hot-pressed ones. Additionally, in view of concrete device implementation, the often overlooked role of cell casing materials was explicitly addressed. Specifically, the galvanic coupling among electrode material, current collector and cell casing was positively measured and rationalized. By integrating innovations in slurry formulations, electrode design, and practical testing setups, this work provides guidelines to transfer nanostructured Zn anodes to the practical device environment.

1. Introduction

The global transition toward sustainable and resilient energy systems is accelerating the demand for alternative electrochemical storage technologies that are safe, cost-effective, and environmentally friendly. While lithium-ion batteries currently dominate the rechargeable battery market, their reliance on critical materials, safety concerns, and limited scalability in certain applications have motivated the exploration of alternative chemistries. Zinc-based battery systems, such as Ni—Zn, Ag—Zn, Zn–MnO_2, and Zn–Air, have emerged as promising candidates thanks to their use of Earth-abundant materials, compatibility with aqueous electrolytes, and practical specific energies ranging from 80 to 475 Wh/kg. However, the widespread deployment of these technologies remains hindered by poor anode cyclability, primarily due to shape changes, hydrogen evolution, and passivation phenomena.

To address these challenges, we previously proposed a nanostructured zinc anode using carbon-coated ZnO nanoparticles (ZnO@C) as active material. [1]. This approach mitigates passivation by maintaining a uniform reaction interface and reduces zincate dissolution through the carbon shell, enhancing anode stability in alkaline electrolytes. Downsizing to the nanoscale also improves ion transport and reactive surface area, overcoming limitations observed in three-dimensional (3D) zinc sponge anodes, such as passivation at high depths of discharge (DOD) and reduced volumetric capacity [[2], [3]]. While the use of ZnO@C as an anode material has been previously demonstrated, most of those studies focused primarily on material

* Corresponding author.
E-mail address: elisa.emanuele@polimi.it (E. Emanuele).

https://doi.org/10.1016/j.jelechem.2025.119653
Received 5 September 2025; Received in revised form 3 November 2025; Accepted 12 November 2025
Available online 15 November 2025

synthesis and idealized testing conditions.[[4–7]] Recent studies have emphasized the critical trade-off between depth of discharge (DOD_{Zn}), cycle life, and specific energy in Zn anodes [[8], [9]]. While low DOD_{Zn} (~10–15 %) values extend cycle life, they limit specific energy to levels comparable to those of lead-acid batteries. Conversely, achieving deeper discharge (40–95 % DOD_{Zn}) improves energy density but shortens cycle life. Therefore, advanced Zn anode designs should yield DOD_{Zn} as high as 75 %–95 %. Maintaining the Zn nanoparticle size throughout charge–discharge could be a possible solution [[10], [11], [12], [1]] to achieve this goal, and doing so will require a tandem approach, combining the physicochemical benefits of nanoengineered ZnO active material with optimized slurry composition and electrode architecture.

The formulation of zinc slurry anodes and the thickness of the active layer play a crucial role in balancing mechanical integrity, conductivity, and electrochemical performance. Typical anodes combine 60–80 wt% Zn-based material, 10–20 wt% conductive additives, and 2.5–15 wt% binders [13]. While thicker electrodes increase energy storage by accommodating more active material, they also introduce challenges, typically higher ionic resistance, that can lead to lower utilization of the active material - the bulk of the electrode not being be fully utilized, and uneven current distribution, which can lead to issues such as dendrite formation [14]. Optimizing electrode formulation - by adjusting the slurry composition, including conductive additives and binders - thickness and casting method involve the complex task of balancing active material loading with efficient ion and electron transport. [15]

Recent interest in shifting toward water-based binders, driven by environmental concerns, tends to replace to PVDF binder and the use of teratogenic organic solvents like NMP with water processable alternative binders such as PTFE and CMC [[16] [17] [18]]. PTFE represents an interesting middle ground in terms of environmental impact. While it can be processed in water, reducing the need for organic solvents, its fluorinated nature and requirement for hazardous wetting agents still pose environmental concerns [19]. However, PTFE offers unique and complementary properties, easily mixing with zinc oxide powder, filling the pore spaces and imparting hydrophobicity to the electrode [20]. In fact, hydrophobicity, while potentially limiting electrolyte accessibility, can help control the excessive swelling that might occur with CMC alone [13]. In turn, CMC offers different, but highly desirable characteristics since its hydroxyl and carboxyl functional groups facilitate strong hydrogen bonding with the active material particles, enhancing mechanical stability and adhesion [19]. Additionally, CMC has been demonstrated to act as an effective inhibitor of zinc corrosion and dendrite growth [20] [21]. However, CMC-based electrodes can become extremely brittle after drying, potentially leading to cracking and peeling of the electrode layer [17]. In fact, brittleness can be particularly problematic when aiming for high active material loadings and long-term cycling. Recent studies, both on Zn anode slurry preparation [[22] [19]] and on MnO_2 cathode slurry formulation demonstrate the complementary effects of combining CMC and PTFE as binding agents. On the one hand, Zn anode performances were reported to increase notably. On the other hand, while PTFE-based electrodes with graphene/MnO_2 allow excellent cycling stability (94 % capacity retention after 3000 cycles) and CMC-based electrodes with MnO_2 provide high initial capacity (294 mAh g^{-1}), their combination offers an optimized balance of both properties [16,20].

A preliminary study from our group screened different PTFE/CMC ratios, showing that higher CMC content improved nanoparticle availability during charge [23]. The present work builds on those findings, applying an optimized binder composition (PTFE 3 %, CMC 12 %) to ZnO@C nanoparticle anodes and focusing on the influence of electrode architecture and fabrication method.

In this scenario, we addressed critical challenges in the development of zinc-based batteries by optimizing zinc anode slurry formulations. Specifically, we investigated the use of PTFE and CMC as complementary binders to enhance mechanical integrity, wettability, ZnO reduction during formation and zinc utilization during discharge, while simultaneously minimizing the use of fluorinated binders.

In the literature, ZnO@C-based anodes have been developed following two main fabrication approaches, reflecting different application targets and coping with trade-offs between capacity and stability. The first category comprises *thin coated electrodes* [[7,10–12]], typically prepared by blade coating or drop casting ZnO@C slurries onto metallic foils such as Ni, Cu, or Sn. These architectures allow high surface utilization and fast ionic access, but their areal loading and mechanical robustness remain limited.

The second category includes *pressed-paste electrodes* [[4–6]], obtained by pressing the slurry composite onto metallic meshes or foams. These systems enable higher mass loading and improved mechanical integrity, but suffer from increased tortuosity and transport limitations that can accelerate passivation and performance decay.

In this work, we compared the influence of electrode architecture by employing two fabrication routes: *blade coating* for thinner electrodes (≈10–100 μm), referred to as **BC-ZnO@C**, and *hot pressing* for thicker ones (≈400 μm), referred to as **P-ZnO@C,** representing the two main fabrication families reported in the literature (table S1). The electrochemical performance and durability of these electrodes were systematically assessed under identical conditions.

Electrochemical measurements were conducted in full-cell Zn/Ni configuration using a commercial Ni/NiOOH cathode, with 100 % DOD of the Zn anode and a coin cell geometry designed for low electrolyte amounts, without additives or saturated ZnO electrolytes, to unambiguously single out the impact of ZnO nanofabrication, while emulating practical device configuraion and cycling conditions.

This approach addresses critical limitations observed in the state-of-the-art Zn-secondary battery research. Notably, many published studies rely on an excess of electrolyte, which can mask the challenges posed by ongoing side reactions, such as electrolyte decomposition accompanied by gas evolution at both electrodes. Furthermore, as reported by Stock et al. [[8]], approximately 50 % of the literature employs Zn-containing salts in the electrolyte to reduce the solubility of the discharge products and mitigate shape changes in anode morphology. While effective in stabilizing the system, the addition of Zn-containing salts introduces an extra capacity (Q_E) that should be calculated ($Q_E = z\ Fc_{Zn}V$). By deliberately excluding these additives and working under low-electrolyte volume conditions, our study offers an unbiased and realistic evaluation of battery performance, providing insights that are directly relevant to practical applications and demonstrating a significant advancement over previously reported configurations. Furthermore, we explicitly addressed the scarcely documented problem of current collector and cell casing selection: material choices that can play a crucial role in device functionality and can be guided by clear electrochemical considerations.

This study also incorporates post-mortem analysis using lab-based X-ray computed microtomography (XμCT) analyses to non-destructively investigate the structural and morphological evolution of the electrodes after cycling. XμCT enables 3D visualization of the electrode microstructure and internal interfaces without dismantling critical components such as the separator. This is particularly important for the detection of features like zinc dendrites, which typically form at the micron scale [24] and can penetrate the separator. Traditional post-mortem methods risk removing or damaging these fragile structures during disassembly, potentially compromising the accuracy of the analysis. By preserving the cell architecture, X-ray CT provides more reliable insight into degradation mechanisms, including the distribution and accessibility of ZnO particles, electrode homogeneity, and dendritic growth. These insights were instrumental in confirming the superior structural integrity and uniform utilization in blade-coated electrodes compared to the heterogeneous and partially unreacted structure observed in hot-pressed ones.

Taken together, these design choices reflect a deliberate effort to move beyond idealized testing conditions and bridge the gap between materials-level optimization and real-world battery deployment. By integrating sustainable electrode formulations, scalable fabrication

methods, and system-level considerations, this work contributes to the advancement of zinc-based batteries as viable components of next-generation electrochemical power systems for renewable energy integration and smart grid applications.

2. Materials and methods

2.1. Synthesis of ZnO@C NPs

The ZnO@C NP synthesis protocol adopted in this work is elaborated on the bases of our previous work [(1)].

The reaction mixture was prepared in a 20 ml quartz reaction vial (G30, by Anton Paar) equipped with a magnetic stirrer, and then sealed with a cap.

0.5 g of sucrose [$C_{12}H_{22}O_{11}$, Sigma-Aldrich 99.5 %] and 0.4 g of zinc acetate dihydrate [$Zn(CH_3COO)_2 \cdot 2H_2O$, Sigma-Aldrich 99.99 %] were mixed in 9 ml ethanol. The vial was then placed inside the microwave reactor (Anton-Paar Monowave 450) and the reaction was carried out using the fast-heating mode at 150 °C with an hold time of 150 min under stirring. Once the process is finished, NPs are filtered and washed with DI-Water and pure ethanol three times, then dried for 4 h in a vacuum oven at 80 °C. After drying, the NPs were subjected to pyrolysis in N_2 atmosphere for 5 h at 550 °C. Typical yield: 19 mg ZnO@C per vial (≈11 % of theoretical ZnO; ≈12 wt% C by TGA).

2.2. Slurry preparation and electrode fabrication

Synthesized ZnO@C was mixed with carbon black (10 %) PTFE (3 %) and CMC (12 %). As prepared Slurry was then:

(i) **P-ZnO@C electrode:** grinded manually in an agate mortar, obtaining thick and viscous slurry that was let it dry at room temperature overnight and then then pasted as a pellet. The self-stand pellet was then pressed at room temperature at 1000 psi for 1 min with a laboratory Hydraulic press (YLJ-HP88 V-350.) and at 1000 psi at 80 degrees for five minutes on a SS mesh.

(ii) **BC-ZnO@C**: Placed in a ball miller jar for a total of 2 h at 250 rpm in a laboratory planetary ball mill. The slurry was then casted onto Cu foil (8 μm, Heliume Tech) with a Doctor blade and dried at room temperature overnight. The electrode is then hot pressed at 80 °C for 3 min at 1000 psi and 1 min at 3000 psi, respectively.

2.3. Ni/NiOOH cathode extraction

Full cells were assembled using Ni/NiOOH, cathodes extracted from Ni-MH AA-energizer 2000mAh commercial batteries through a carefully controlled procedure to preserve their structural and electrochemical integrity. The batteries were first discharged at a C/10 rate to a cutoff potential of 0.15 V to minimize the risk of short-circuiting during subsequent handling and disassembly. Following discharge, the battery casing was removed using a handheld precision Dremel. The cathode material was extracted from the top of the cell, unrolled, and cleaned with deionized water (DI-W). To enhance the mechanical stability and ensure uniform surface characteristics, the extracted cathode was subjected to two pressing protocols: cold pressing at 500 psi for 1 min, followed by hot pressing at 80 °C for 5 min at 500 psi.

2.4. Electrochemical measurements

2.4.1. Cyclic voltammetry (CVs)

CVs were performed in a three-electrode cell (497 universal cell, AMEL), using an Hg/HgO reference electrode (AMEL 383/OHG/12, 0.1 M KOH) a 0.9 cm^2 platinum counter electrode (CE) and the working electrode, prepared as described in Section 2.2 (i) with a mass loading of 110 mg cm^{-2}.

The cell contained 40 mL of 6 M KOH, which was degassed by N_2 bubbling (0.5 $nLmin^{-1}$, 30 min), to avoid ORR current background, before running the experiment, and kept under a blanket of flowing N_2 during the electrochemical measurements. CVs were performed with a VMP-300 BioLogic potentiostat/galvanostat at 1 mVs^{-1}. At the end of each measurement, an aliquot of fresh electrolyte was employed. The RE and all the cell components were thoroughly washed the deionized water.

2.4.2. Galvanostatic charge-discharge cycles (GCD) and battery assembly

To ensure comparability with previous studies [10–12], we tested our materials a using 2032-coin cell configuration. However, to gain better geometrical control on cell mounting, we resorted to using a split cell (ELL CELL) (cell components reported in Fig. S6), emulating the CR 2032 electrode arrangement and using a Pt wire as pseudo reference electrode. In particular, the split cell setup allows better control over electrode positioning and applied pressure, leading to improved reproducibility of measurements. Additionally, its easy disassembly facilitates post-mortem electrode analysis after cycling. While many studies have relied on beaker-type configurations with excess electrolyte, these setups deviate from technologically relevant conditions, as discussed in the introduction. Our approach ensures both analytical rigor and practical relevance in material battery testing.

2032-coin cells were assembled under atmosphere environment with the can at the bottom, followed by the ZnO@C anode, 100 μL electrolyte of 6 M KOH, glass fiber separator (GF 6, Whatman) then an excess (≯ 90 %) of the Ni/NiOOH extracted cathode, Ni sponge current collector, spring and cap were placed respectively. 300 and 250 μm thick Pb and Zn foils, respectively, were used as spacers in the coin cell-assembly of Fig. 4.

Split cells were assembled following the same order of coin cells. A stainless-steel mesh was used as the current collector just for self-stand **P-ZnO@C** anode and the same glass fiber separator (GF6 Whatman) was wetted with 100 μL of 6 M KOH. The same extracted Ni/NiOOH was then used with a Ni sponge as the current collector. Also, for the BC-ZnO@C electrodes, the Cu foil used for the coating was used as the current collector. The mass loading of the active material in **P-ZnO@C** and **BC-ZnO@C** is on average 72.3 mg and 1.96 mg, respectively.

Two types of charging protocols were investigated for **P-ZnO@C** and **BC-ZnO@C** anodes. Specifically, we followed the same cycling protocol reported in [10–12], cells were galvanostatically charged to the theoretical capacity of ZnO (658.5 mAh g^{-1}) and discharged to a cut off of 1.35 V, at 1C. A Charging voltage cut-off of 2.1 V was set to limit electrolyte degradation.

Additionally, we tested a potential-limited cut-off (S3), where the charge was terminated solely by a voltage rather than a capacity set-point. The results of this second set of experiments are provided in the Supplementary Information (SI). However, the most effective charging protocol was found to be the capacity-limited approach, that enables better control of recharge completion.

The **P-ZnO@C** anode was charged and discharged to 10 % DOD and DOC, as commonly used in the literature [8,9]. The obtained specific discharge capacity was calculated considering 10 % of the active mass loading. In contrast, **BC-ZnO@C** anodes were cycled with a higher active material utilization, using a DOD and DOC of 100 %. The carbon content of the ZnO@C nanoparticles, determined by TGA under air, was ≈12 wt% as reported in section 2.1. Specific capacities were calculated with respect to the ZnO mass only, excluding the carbon fraction.

For bulk Zn foil battery testing, Zn foil (0.25 mm, goodfellow) was used as the anode while the other battery parts remained the same and the GCPL test was performed with 2 mAh at 1C.

2.5. Materials characterization

In order to investigate the morphological and microstructural changes occurring during electrochemical cycling, a post-mortem analysis was carried out on a selection of full cells by using 3D XμCT

imaging.

2.5.1. X-ray computed microtomography (XμCT): Experiments and data processing

The XμCT measurements were performed by using the EasyTom XL Ultra 160–230 scanner (RX Solutions, France) located at the Department of Materials of the Slovenian National Building and Civil Engineering Institute (ZAG, Ljubljana). The scanner is equipped with an open nanofocus X-ray source combined with a tungsten (W) transmission target. The source can operate in a voltage range of 20–160 kV and at a maximum power of 32 W. Samples are installed on the top of a high-precision air-bearing rotation stage. A 16-bit, (2560 × 2048) pixels^2, flat panel detector with a pixel size of (124 × 124) μm^2, corresponding to a field of view (FOV) of 317 mm × 253 mm, has been used to acquire a set of radiographs (projections) of the sample ad different angular views. The highest achievable spatial resolution of the employed set up is 0.8 μm. To enhance the visibility between the phases of interest in the sample and reduce noise, the projection images were acquired in propagation-based phase contrast mode ([25]).

Samples were four [4] circular cells (max Ø: 18 mm) wrapped in Parafilm® and fixed with the flat circular faces perpendicular to the rotation stage. A set of 1984 projections has been acquired during a continuous 360° rotation working in region of interest modality (sample larger than the detector FOV). An Al filter with a thickness of 1 mm was placed between the X-ray source and the sample in order to reduce beam hardening effects. For each scan, an acquisition of 1 frame per second (Fps) and 8 frames averaged was set corresponding to a total duration of each scan of approx. 4.5 h.

The sample names, their description, as well as the main XμCT scanning parameters are reported in Table 1.

The tomographic reconstruction, allowing to obtain the axial slices of the sample volume illuminated by the X-ray beam, was performed using the commercial X-ACT software (RX Solutions). The same software was used to remove eventual artefacts present in the images (e.g. ring artefacts, beam hardening correction) and for phase retrieval. The latter procedure was applied to the projection images using the Paganin's algorithm (Paganin et al., 2002).

After reconstruction, the bi-dimensional (2D) virtual section of the sample was visualized using the open source Fiji software (Schindelin et al., 2012.) while the three-dimensional (3D) visualzaton was obtained through volume rendering procedures, using the commercial software Dragonfly (Comet, Canada.

3. Results

The individual electrochemical performances of the separate ZnO NPs-based anodes and the Ni/NiOOH cathode were first evaluated using CVs (Fig. 1A) in a three-electrode cell at a scan rate of 1 mV s^{-1}. GCD measurements were then performed in both the cell setup used for CVs (Fig. 1B) at C/50 and the split cell configuration, using a Pt pseudo-reference electrode at C/5 (Fig. 1C,D).

The redox behavior of the as-fabricated P-ZnO@C anode in the cathodic branch is characterized by an initial current density increase with a cathodic peak (c) located at −1.7 V vs Hg/HgO, associated with the charge-transfer process corresponding to ZnO reduction to Zn via intermediate zincate formation [[26]]. The cathodic current remains stable across cycles, indicating that the carbon shell in the electrode effectively suppresses ZnO dissolution in the alkaline environment, thus preserving the active material during cycling.

The anodic scan in the CV is characterized by two anodic peaks, suggesting the presence of multiple electrochemical processes during the oxidation of zinc. The first anodic peak (a), observed at approximately −1.1 V, corresponds to the direct oxidation of metallic zinc to soluble zincate ions ($[ZnOH_4]^{2-}$). The *sec*ond peak (b), at a higher potential −0.9 V, is usually typical of an actively corroding system with the accumulation and transformation of Zn-based corrosion products such as $Zn(OH)_2$ and polymeric Zn–OH species, formed as the local zincate concentration increases [1],

At higher potentials, a sharp anodic spike is observed, which can be attributed to the breakdown of the transient $ZnO/Zn(OH)_2$ passive layer and the reactivation of the metallic Zn surface.

As far as the cathodic material is concerned, CV scans were used to evaluate the activity after the extraction from commercial cells, as specified in Section 2.3. The redox behavior in the anodic branch is characterized by an initial increase in current density with an anodic peak (d) located at 0.25 V, that corresponds to NiOOH formation through oxidation of Ni/NiOOH. Continuing the anodic-going scan, a second increase in current densities is then observed, related to oxygen evolution reaction. The cathodic-going scan reveals a broad reduction peak (e) located at 0.1 V, associated with the conversion of NiOOH back to $Ni(OH)_2$. The peak potential positions were used to evaluate the charging potential cut-off used in potential limited GCD cyclings (fig. S3 of SI). Galvanostatic measurements at C/50 showed that the cathode material, exhibited a discharge capacity of 39 mAh (Fig. 1B). By comparing this result with the theoretical capacity of Ni/NiOOH [27,28], the percentage of active material in the commercial slurry formulation was estimated.

Alkaline Ni − Zn full cells were then assembled with excess (≈ 90 %) $Ni(OH)_2$ cathodic material using a split-cell set-up. GCD curves of the full cells with P-ZnO@C electrode following the potential of both electrodes with Pt pseudo reference are presented in Fig. 1C and Fig. 1D. Charge/discharge plateaus around −1.55 and − 1.45 V can be observed in the GCD curves for the P-ZnO@C electrode, consistent with the CV result. The voltage difference between charge and discharge is around 100 mV, indicating a rather low polarization and, in particular, fast charge-transfer kinetics.

Subsequent to electroanalytical chacaterization of the individual electrodes, the electrochemical stability of P-ZnO@C and BC-ZnO@C anodes were then evaluated through prolonged GCD cycling in two-electrode configuration, in split- set-ups. At variance with similar literature studies, this choice is motivated by the fact that we meant to test the electrodes in a realistic battery configuration, in which the amount of electrolyte is limited. In addition, as put forward in introduction in order to test the real response of ZnO NPs, without interference of Zn(II) the electrolyte adopted was pure 6 M KOH, without either ZnO or other additives.

These cells were galvanostatically charged to the theoretical capacity of ZnO (658.5 mAh g^{-1}) and fully discharged to 1.35 V at 1C rate (more details in Section 2.3.2).

Fig. 2a and 3a compares the specific capacity of the BC-ZnO@C and

Table 1
Sample names, their description, and the main XμCT scanning parameters.

Sample name	Sample description	Imaging conditions				
		SOD/SDD (mm)	Voltage [V]	Power [W]	Pixel size [μm]	Frames per sec, averaged frames
Aged BC-ZnO@C	Full-cell with Blade-coated anode after cycling	21.6/1125.6	130	11.6	2.38	1 Fps, 8
Pristine BC-ZnO@C	Full-cell with Blade-coated anode before cyclin	21.6/1122.9	130	11.6	2.38	1 Fps, 8
Aged P-ZnO@C	Full-cell with hot-press anode before cycling	21.6/1122.9	130	12.0	2.38	1 Fps, 8
Pristine P-ZnO@C	Full-cell with hot-press anode before cycling	21.6/1122.9	130	12.0	2.38	1 Fps, 8

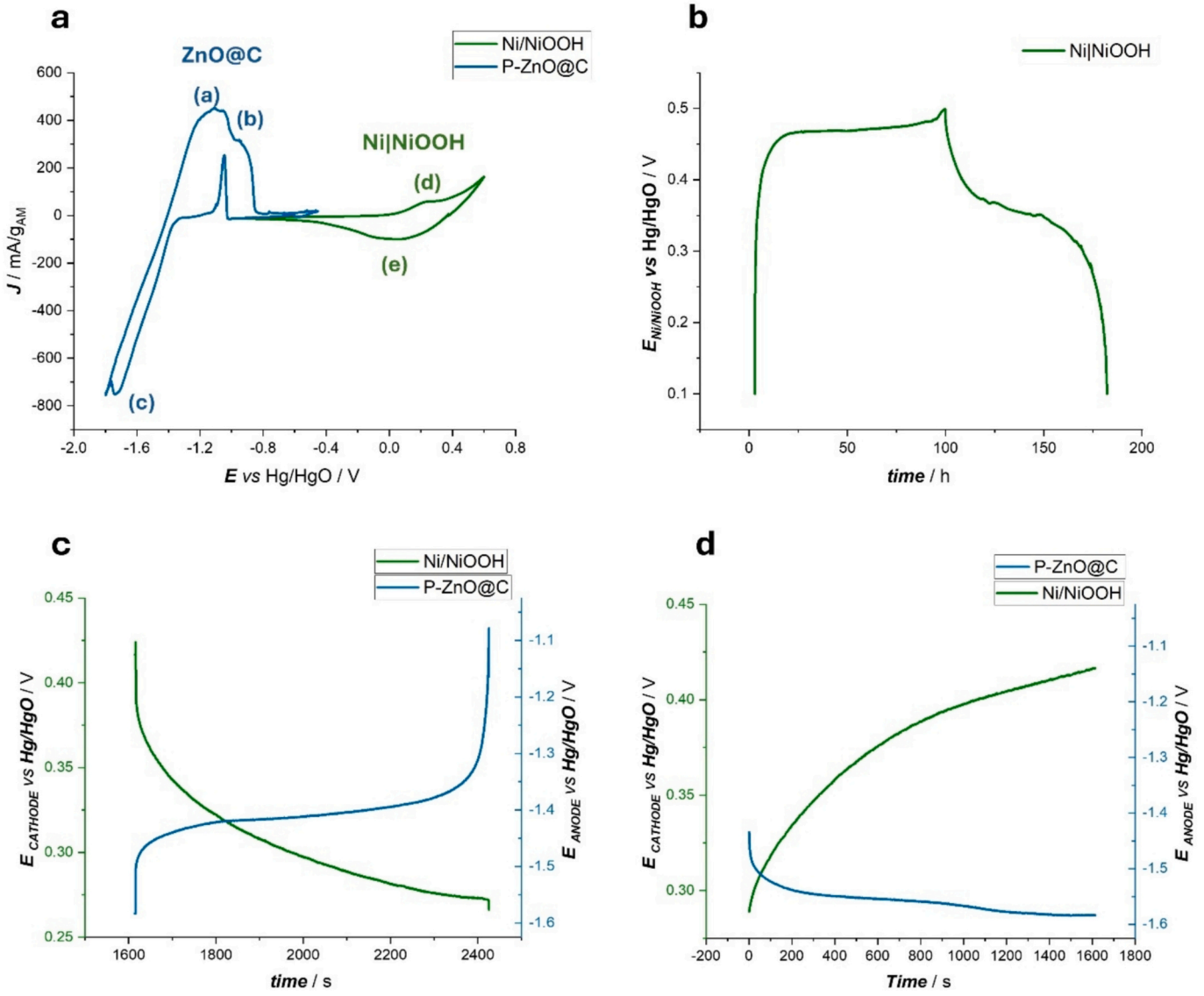

Fig. 1. (a) CV of Ni/NiOOH and ZnO@C electrodes (scan rate 1 mV s^{-1}). (b) GCD cycling of Ni/NiOOH commercial cathode in a three-electrode configuration with Zn foil counter electrode (C/50). Charge (c) and discharge (d) of P-ZnO@C anode and Ni/NiOOH cathode in Split cell (C/5).

P-ZnO@C anodes, with average mass loadings of the P-ZnO@C and BC-ZnO@C active materials of 72.3 and 1.96 mg cm^{-2}, respectively. For comparison, a cell of the same type was assembled using bulk Zn foil under identical testing conditions discharging it to just 1 % DOD. The performance of the Zn foil electrode, represented by the black points in Fig. 2a and 3a, exhibited stable behavior for only 14 cycles before rapid capacity decay to zero, attributed to passivation. In contrast, the P-ZnO@C (Fig. 3a) anode sustains 50 cycles before experiencing significant capacity degradation, demonstrating that, as expected [1], reducing particle size alongside the carbon shielding of the ZnO particles effectively mitigates passivation.

Moreover, electrode BC-ZnO@C (Fig. 2a), exhibiting a limited active layer thickness, shows a significantly better performance that Zn foil, allowing more than 160 cycles above 400 $mAhg^{-1}$. Instead, the pasted electrode exhibits a rapid decline, losing half of its initial energy storage capacity, while the blade coated electrode displays a much slower rate of decay and a substantially longer cycle life. This can be clearly seen in the specific discharge capacity at the 88th cycle, as reported in the plot of Fig. 2b and 3b. The enhanced performance is likely due to optimized electrode architecture, leading to better ZnO@C particle accessibility and more efficient electrochemical reduction during charging.

In particular, detailed inspection of the GCD cycles shows that the voltage profiles of P-ZnO@C (Fig. 3b) demonstrated consistent one-hour charging cycles at higher potential then the BC-ZnO@C one throughout the testing duration.

Initial cycles of BC-ZnO@C demonstrated efficient energy retention, evident in the discharge capacity-voltage profiles shown in Fig. 2b. The discharge-specific capacity reached a maximum of 524 $mAhg^{-1}$, corresponding to approximately 80 % of ZnO theoretical capacity. Notably, BC-ZnO@C anode maintained a discharge-specific capacity exceeding 400 $mAhg^{-1}$ for more than 200 cycles, although a gradual decline in cycling efficiency was observed (Fig. 2b). To better place in context these results, a comparative summary of the most recent ZnO@C anode studies was compiled (Table S1, Supporting Information).

Previous work was performed in ZnO-saturated [4–7] and/or additive-containing electrolytes [7,10–12](e.g., Bi_2O_3, In_2O_3, SnO, KF, or K_2CO_3), which strongly suppress hydrogen evolution and Zn dissolution. Under these artificially favorable conditions, specific capacities between 300 and 500 mAh g^{-1} are commonly reported over 100–200 cycles, after which progressive capacity fading is usually observed.

In contrast, the present BC-ZnO@C electrode, tested in additive-free and ZnO-free 6 M KOH and in a sealed coin-cell configuration, delivers

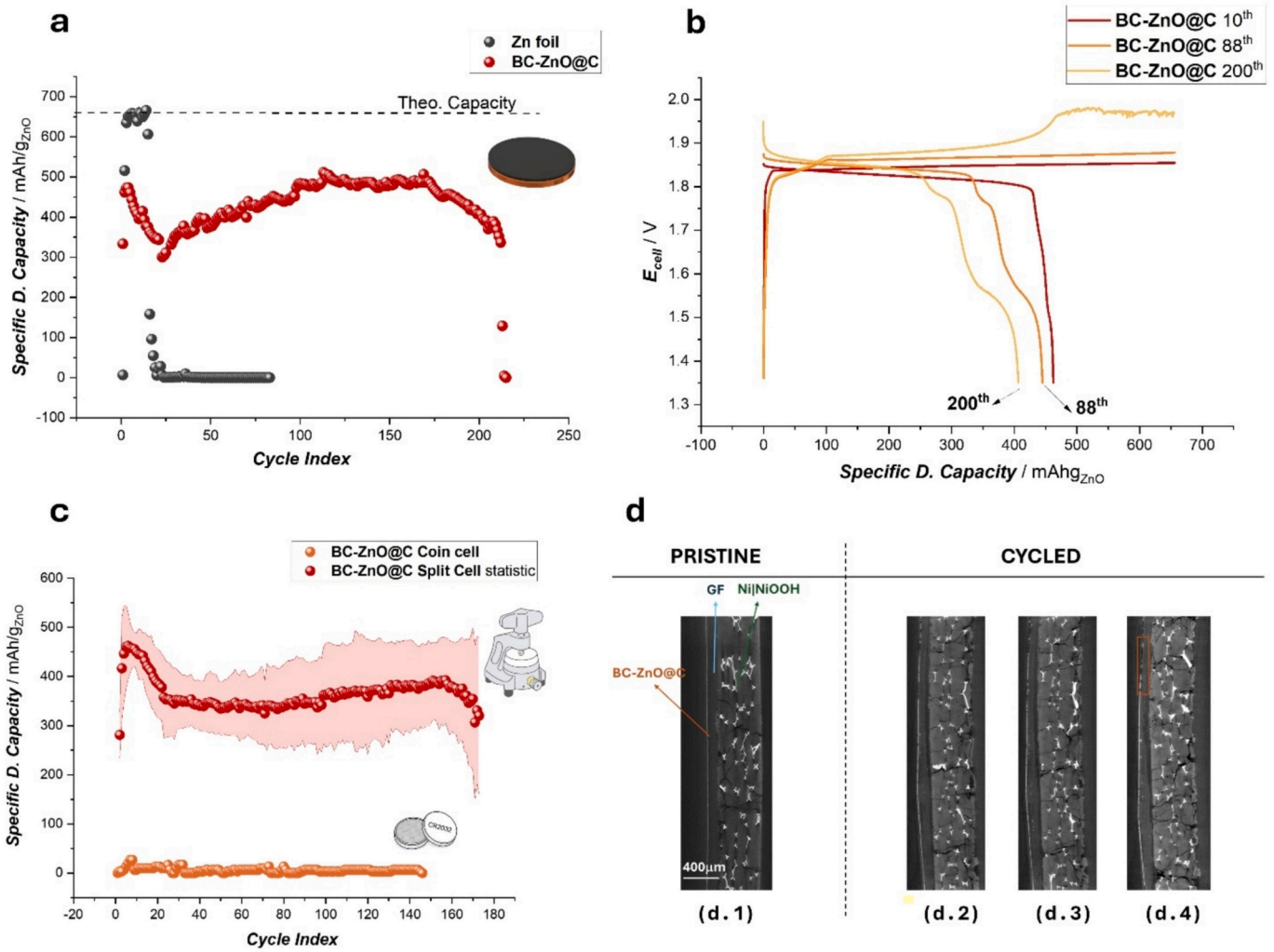

Fig. 2. (a) GCD cycling response at 1C rate of Zn—Ni full cells with of BC-ZnO@C with 100 % DOD (red), and Zn foil with 1 % DOD (black) anodes. Cycling has been carried out in split-cells. The theoretical capacity of ZnO is indicated with a dashed black line. (b) Voltage profiles at 10th, 88th, and 200th, cycles of BC-ZnO@C shown in panel A vs Specific Cpacity. (c) GCD cycling response at 1C rate of Zn—Ni full cells with of BC-ZnO@C with 100 % DOD cycled in coin cell and Split cell configurations. The split-cell data are presented as mean values with standard deviation (error bars) obtained from multiple independent measurements reported in S1. (d) Virtual cross-sections obtained by XμCT analyses showing the copper current collector, the **BC-ZnO@C** anode (orange arrow), the GF- separator (blue arrow) and Ni/NiOOH cathode (green arrow) of pristine (d.1) and aged (d.2, d.3, d.4) cells. (For interpretation of the references to colour in this figure legend, the reader is referred to the web version of this article.)

an initial capacity of ≈ 500 mAh g^{-1} and retains ≈ 400 mAh g^{-1} after 200 cycles, i.e. comparable or superior to those reported in the literature for ZnO-containing electrolytes.

The charge-discharge efficiency decay is correlated with signal noise present at a potential of 1.95 V during the final stage of charging. Indeed, this second plateau can be linked to an enhanced HER side reaction which limits the conversion of ZnO to metallic Zn. Recent studies have proposed innovative approaches to overcome the intrinsic transport and mechanical limitations of high-loading electrodes, including hierarchical porosity design and conductive network optimization [[29,30]]. These works demonstrate that balancing mechanical robustness and ionic accessibility is essential to achieving high utilization of active material under practical conditions. In this context, our results confirm that the blade-coated ZnO@C electrodes, with limited active layer thickness and homogeneous architecture, provide a favorable balance between loading and utilization efficiency, while the thicker hot-pressed electrodes suffer from transport limitations similar to those reported in other high-loading systems.

In the previous analysis, presented in Fig. 2a and 3a, GCD cycling in split cell configuration demonstrated consistent and reliable (replicated measurements are reported in Fig. S1 and S2) electrochemical behavior, providing initial insights into the system stability and performance. Building on this, further investigation on BC-ZnO@C and P-ZnO@C anodes was conducted using both coin cell (2032), following the procedure detailed in Section 2.3.2 (Fig. 2c and 3c).

The split cell configuration exhibited superior electrochemical performance, achieving higher specific capacity values and enhanced cycling stability compared to the coin cell arrangement. The reduced Specific Capacity observed was found to be more pronounced for BC-ZnO@C. Galvanic coupling in the coin cell system, arising from the interaction between the stainless steel (SS) casing and current collectors, can leads to the dissolution of metal impurities poisoning the anode active material.

To investigate it in more detail we carried out GCD experiments in the coin cell system with a range of candidate metals (Fig. 4) aiming at elucidating galvanic coupling effects rather than ranking current collectors by performance. In the split cell, which features a plastic casing and a thin (2 mm), a Au pin electrode connection is positioned at the centre of bottom of the plastic casing hoisting the working electrode. With this configuration, electrolyte access to the Au pin is restricted and

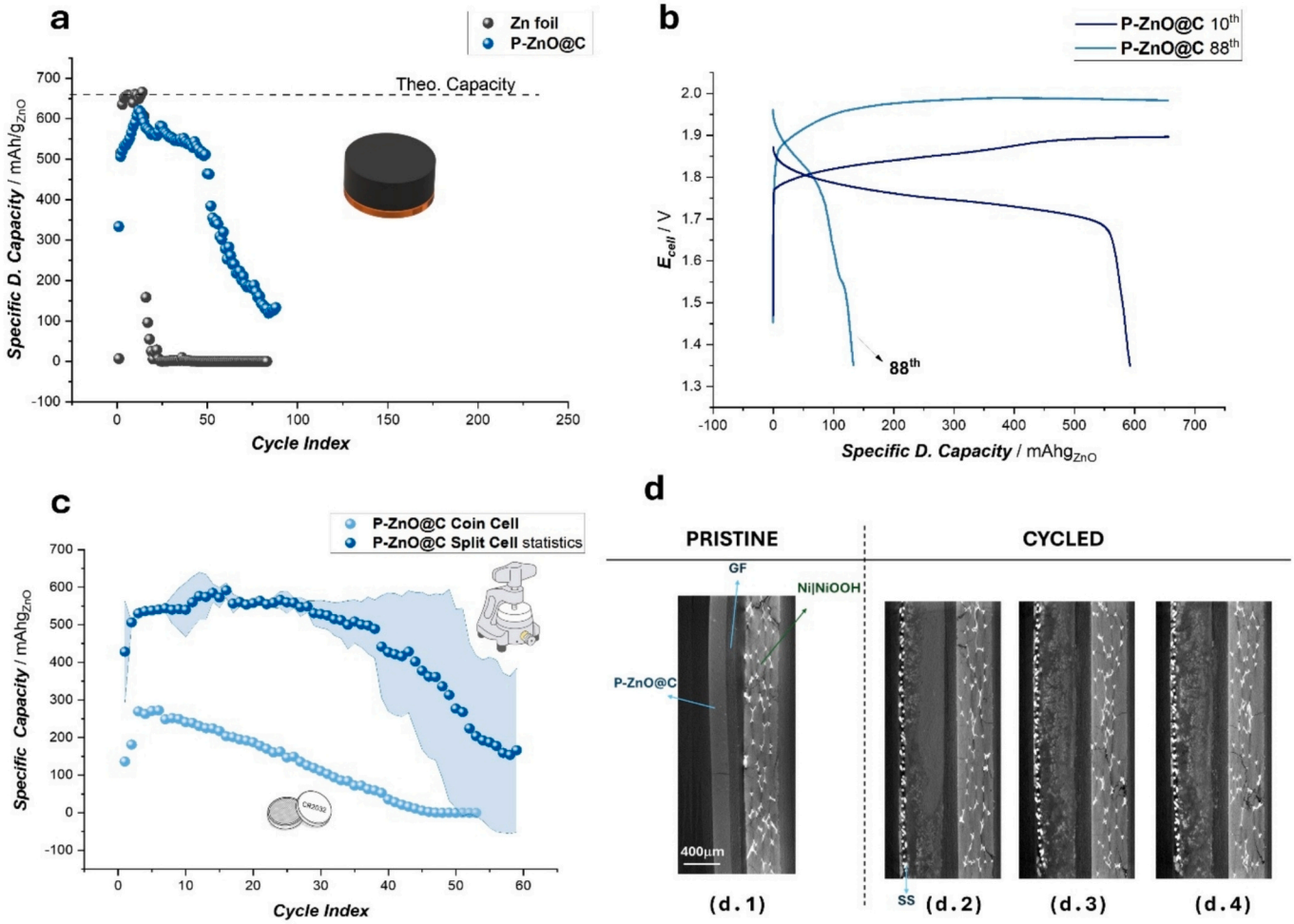

Fig. 3. (a) GCD cycling response at 1C rate of Zn—Ni full cells with of P-ZnO@C with 10 % DOD (blue) and Zn foil with 1 % DOD (black) anodes. Cycling has been carried out in split-cells. The theoretical capacity of ZnO is indicated with a dashed black line. (b) Voltage profiles at 10th, 88th cycles of P-ZnO@C shown in panel a vs Specific Cpacity. (c) GCD cycling response at 1C rate of Zn—Ni full cells with of P-ZnO@C with 10 % DOD cycled in coin cell and Split cell configuration. Presented as mean values with standard deviation (error bars) obtained from multiple independent measurements reported in S2. (d) Virtual cross-sections obtained by X-ray microtomography showing (d.1) the pristine cell configuration, composed of the self-standing P-ZnO@C anode, glass fiber separator, and Ni/NiOOH cathode, and (d.2–d.4) aged cells after cycling, where the stainless-steel (SS) mesh current collector is visible as part of the anode structure. (For interpretation of the references to colour in this figure legend, the reader is referred to the web version of this article.)

thus galvanic contact between the pin and the working electrode is virtually avoided. This configuration is different from that of a conventional coin cell setup, where the entire case is made of steel, allowing direct and extensive contact with the electrolyte spilling over from the separator. As a result, in split cell the best cycling performance for Cu-supported BC-ZnO@C anodes remained stable over 200 cycles as reflected in consistent specific capacity and *E*-t transients reported in Fig. 2. Instead, the same anode employed in coin cell tests (orange plot), gave rise to serrations in the potential time-serie did not allow to reach and maintain an efficient charging plateau with a midpoint voltage of 1.8 V. This behavior can be straightforwardly explained with the galvanic coupling between the SS coin cell casing and the Cu current collector. In fact, this coupling leads to the corrosion of the Cu collector, generating Cu^{2+} ions that can flow to the ZnO@C electrode and get cemented on electroreduced Zn. Cu cementation onto Zn promotes Zn corrosion and HER, leading to the establishment of a mixed potential below 1.8 V, denoting failure of quantitative Zn formation from ZnO.

To more insightfully assess this multimetallism behavior, we introduced different types of spacers and current collectors. Specifically, a spacer consisting of a metal that is less noble than Cu and SS, such as Zn and Pb imparts sacrificial galvanic protection to both Cu and SS, thus suppressing Cu^{2+} release. The data reported in the blue and light blue plots of Fig. 4 clearly show that the midpoint voltage of charge (1.8 V) can in fact be reached. However, after a few cycles, capacity once again declined, and the cell was unable to reach it. It is worth noting that the same behavior was observed when using bulk Zn foil as the anode material (red plot). This long-term evolution of the cycling time-series can be explained considering similar galvanic coupling effects on the cathodic side of the cell. In fact, contact between SS and Ni induces SS corrosion, resulting in Fe^{2+} release, transport to the anolyte and final cementation on electroformed Zn. This process yields the same effect as Cu cementation, triggered Zn corrosion and HER catalysis, with attending continues Zn consumption and establishment of a mixed potential lower than the midpoint one.

Notably, cycling stability improved when a freestanding P-ZnO@C (i.e. without a current collector) anode (black points) was used instead of a Cu-supported one. This can be explained with the fact that the galvanic coupling between carbon and the SS casing is less active that between Cu and SS and leads to a relatively slower release of Fe^{2+} that eventually cements onto Zn formed at the anode, in combination with Fe^{2+} resulting from the above-mentioned process at the cathode. Recharge failure is delayed in the case of the freestanding anode because of the larger amount of active material available in this electrode.

These measurements underscore the critical role of material

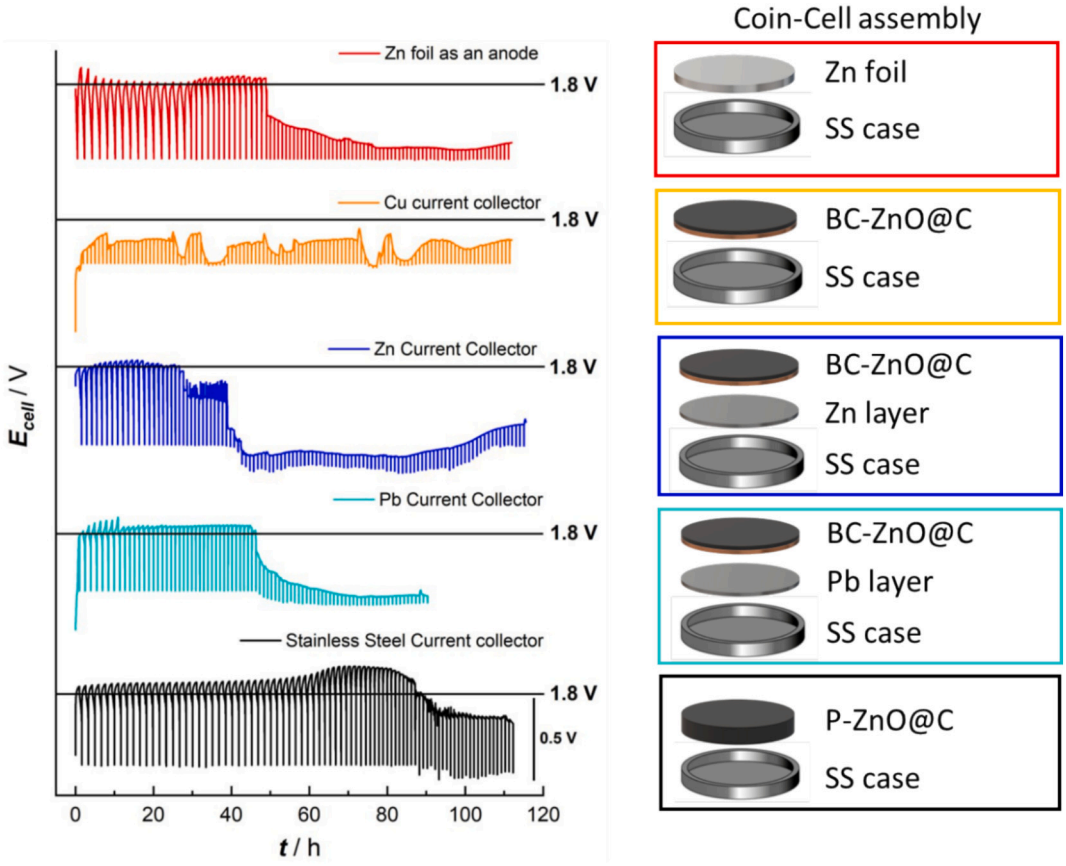

Fig. 4. Galvanostatic charge-discharge profiles (1C, capacity limited charging).

selection and cell design in stabilizing Zn-based battery systems, particularly those prone to galvanic interactions within the cell casing.

comparing different current collector materials in coin cell configuration: Zn foil anode (red), Cu (orange), Zn (blue), Pb (cyan), and SS with freestabding pasted anode (black).

In order to verify the hypothesis of galvanic coupling reported we

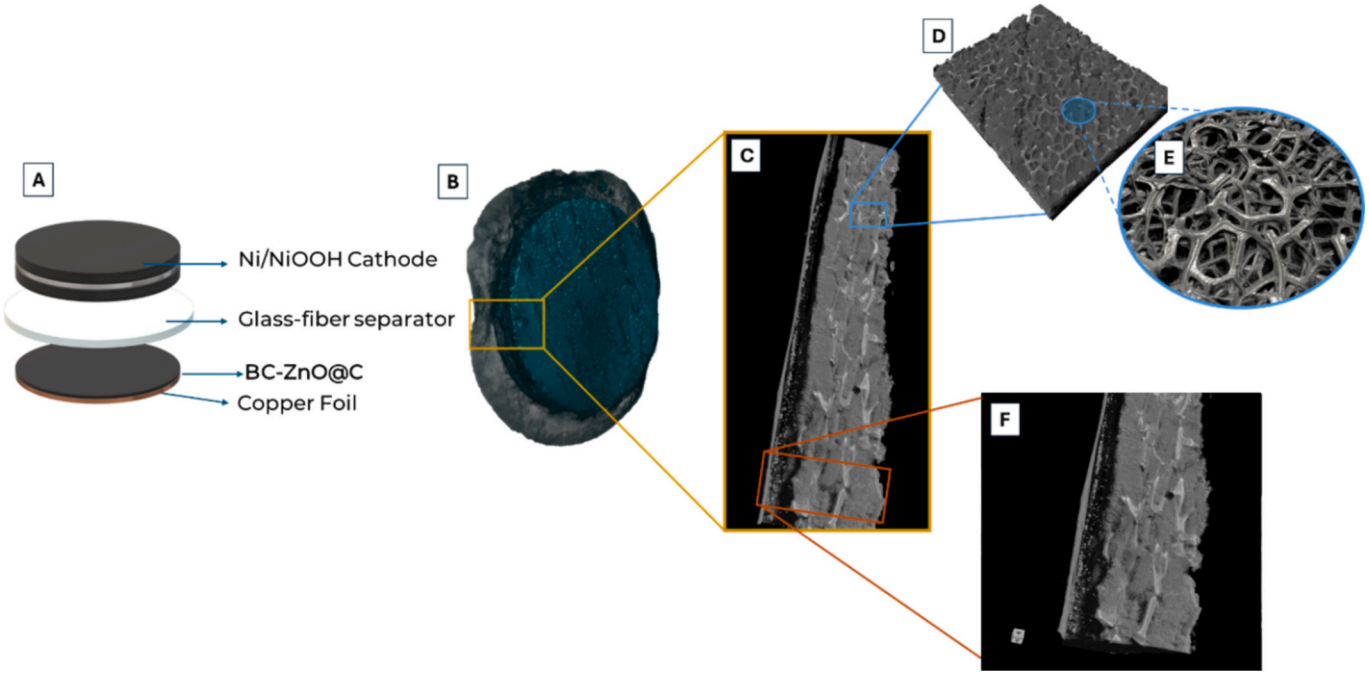

Fig. 5. (A) Schematic illustration of the battery assembly with BC-ZnO@C anode, (B, C) Volume renderings of the reconstructed full battery analysed by X-ray computed microtomography (XμCT) 3D rendering of (D) the Ni/NiOOH cathode and (E) the Ni sponge. (F) 3D rendering showing a portion of the anode and cathode microstructure.

performed ZRA measurements with the metal combinations presented in Fig. 4.

The current-time transients for various metal couples tested are presented in Fig. S4. Specifically, when Cu foil is coupled with the SS casing, a positive current on the order of 8×10^{-7} Acm^{-2}. is observed at Cu (Fig. S4 A), while a corresponding negative current is measured at SS (Fig. S4 B) in the Cu-SS pair. This observation proves the corrosion of the Cu current collector. When Zn or Pb is coupled to Cu or SS, a negative current is recorded (Figs. S4 C—F), indicating that Zn and Pb behave as sacrificial anodes, preventing both Cu and SS corrosion.

Additionally, the coupling between SS and a Ni sponge current collector, used at the positive pole of the battery, was tested. In this case, a positive current of approximately 3×10^{-9} Acm^{-2} was measured (Fig. S4 G), suggesting SS corrosion, with Fe^{2+} release.

The electrochemical performance observed in the GCD cycling tests reported in Fig. 2 highlights the impact of electrode architecture and active layer thickness on capacity retention. A post-mortem XmCT analysis of four full cells allowed us to get a deeper insight into the morphological and structural changes occurring during prolonged cycling, Fig. 5 shows the 3D rendering of the full cell extracted from the split cell set-up, with the assembly scheme presented in Fig. 5A.

Fig. 2d reports representative virtual sections obtained by XμCT analyses of a of full battery pristine cell (Fig. 2 (d.1)) and cycled cell (Figs. 2 (d.2, d.3, d.4)) after the GCD cycling reported in Fig. 2. Distinct morphological and compositional features of the electrode materials are observed. The left side part of the images shows the anodic region, featuring the copper foil current collector (8 μm) and the 150 μm thick blade-coated anodic layer (BC-ZnO@C). Then, the glass-fiber separator is discernible in the central portion of the image, characterized by a lower mass density. In Fig. 2d, the green arrow highlights the region corresponding to the Ni/NiOOH. Bright regions within this section represent the metallic Ni mesh scaffold. The cathode exhibits extensive cracking, likely resulting from mechanical stress after the disassembly of commercial cylindrical AA cell and/or oxygen evolution occurring during charge: an analysis of the details of the cathode behavior is beyond the scope of the present work that is focused on the anode characterization.

In the anode region, spherical bright particles are visible in the cycled sample (Fig. 2(d.2, d.3, d.4)), corresponding to metallic Zn formed via electrochemical reduction/oxidation cycles starting from ZnO nanoparticles. The 3D rendering reported in Fig. 5C better reveals the distribution of these spheroidal particles. Due to the spatial resolution set in the XμCT system employed in order to image a large portion (representative volume) of the full cell, only Zn particles with a minimum size of a few microns can be discerned. Nevertheless, the presence of Zn particles throughout the entire thickness of the electrode indicates uniform reduction of ZnO, witnessing high utilization of the active material.

Images of the aged sample reveal a lack of continuity in the copper film current collector (highlighted by the orange rectangle in Fig. 2 (d.4)), suggesting copper dissolution during cycling. A 3D rendering of the Cu foil, including a magnified view of the pinhole, is presented in Fig. S4 of the SI.

In Fig. 3d representative sequence of XμCT virtual sections of the pristine P-ZnO@C sample (Fig. 3(d.1)) and after GCD cycling (Fig. 3 (d.2, d.3, d.4)) is reported.

TheXμCT image of the pristine sample reveals a well-defined and homogeneous microstructure, with a uniform distribution of pores. The internal framework appears structurally intact, suggesting good mechanical integrity. The pristine sample does not feature the stainless-steel mesh because the electrode is fabricated as a self-standing pellet. Therefore, the current collector is only added during the cell assembly process.

A structural degradation is evident in the aged sample (Fig. 3 (d.2, d.3, d.4)).

Several notable microstructural changes can be observed. A pronounced increase in porosity, particularly along the outer edge near SS mesh current collector can be seen, with an extensive deposition and accumulation of material. Cracking within the electrode structure becomes more evident, indicating buildup of mechanical stress, that can be attributed to periodic volumetric expansion and contraction during cycling. Moreover, cracking can be due to the non-uniform reduction rates within the porous electrode structure, that promote parasitic HER, leading to pressure buildup inside the electrode. Cracks contribute to electronic isolation of active material, negatively impacting electrochemical performance. The images reveal that metallic Zn filaments form at the current collector region of the thick electrode as a result of ZnO nanoparticle reduction, while the ZnO located in some central region remains unreduced (Fig. 3 (d.2)).

In correspondence, the electrode shows poor cyclability even when just 10 % of the active material is used. This behavior is very different from that found in 100 μm thin blade coated electrodes implementing the same active material: here reversible interconversion of Zn/ZnO ensures excellent cyclability even at higher DODs (DOD = 100 %).

The progressive structural changes in aged anodes suggest a correlation between cycling and microstructural degradation. The observed crack propagation and edge deterioration localization lead to reduced mechanical stability, impaired ionic/electronic transport, and performance fade.

4. Conclusions

This study provides a comprehensive evaluation of ZnO nanoparticle-based anodes for alkaline Ni − Zn batteries, focusing on electrochemical performance, degradation mechanisms, and structural evolution during cycling. CV and GCD analyses reveal that the incorporation of a carbon shell effectively stabilizes ZnO nanoparticles, mitigating passivation effects and enhancing charge-transfer kinetics. Prolonged cycling tests demonstrate that electrode architecture and active layer thickness significantly influence capacity retention, with BC-ZnO@C anodes achieving extended cycle life compared to Zn foil and P-ZnO@C.

A *post-mortem* high-resolution X-ray computed microtomography characterization highlights critical degradation phenomena, including copper current collector dissolution and non-uniform ZnO reduction that disclose possible pathways for further improvement of the anode functional properties. The formation of metallic Zn filaments and electrode cracking in thick electrodes further indicate that parasitic HER reactions contribute to capacity fade, particularly in high-loading configurations. The impact of galvanic coupling between Cu and the stainless steel of the coin cell casings was also assessed, causing metal dissolution from the casing and redeposition at the anode surface that, accelerate HER, ultimately affecting long-term cycling stability.

These findings underscore the importance of optimizing electrode composition, architecture, and cell design to enhance the stability of Zn-based batteries. Strategies such as improved current collector materials, and controlled ZnO reduction pathways could further mitigate degradation processes and extend cycle life in practical applications.

CRediT authorship contribution statement

Elisa Emanuele: Writing – review & editing, Writing – original draft, Visualization, Validation, Methodology, Investigation, Formal analysis, Data curation, Conceptualization. **Lucia Mancini:** Writing – review & editing, Validation, Methodology, Investigation, Formal analysis, Data curation, Conceptualization. **Seyedamin Razaghi:** Visualization, Validation, Investigation, Data curation. **Rožle Repič:** Writing – review & editing, Investigation, Data curation, Conceptualization. **Maya Kobchenko:** Writing – review & editing, Investigation, Data curation. **Benedetto Bozzini:** Writing – review & editing, Writing – original draft, Visualization, Validation, Supervision, Resources, Project administration, Methodology, Investigation, Funding acquisition, Formal analysis,

Data curation, Conceptualization.

Declaration of competing interest

The authors declare that they have no known competing financial interests or personal relationships that could have influenced the work reported in this paper.

Acknowledgments

1) Co-funding was received from ZnOrgBat project (no. 23034) under the EIT RawMaterials, part of the Horizon Europe funding scheme. 2) This study was carried out within the MOST – Sustainable Mobility Center activities funded from the European Union Next-GenerationEU (PIANO NAZIONALE DI RIPRESA E RESILIENZA (PNRR) – MISSIONE 4 COMPONENTE 2, INVESTIMENTO 1.4 – D.D. 1033 17/06/2022, CN00000023). This manuscript reflects only the authors' views and opinions, neither the European Union nor the European Commission can be considered responsible for them.

Declaration of competing interest

The authors declare that they have no known competing financial interests or personal relationships that could have appeared to influence the work reported in this paper.

Appendix A. Supplementary data

Supplementary data to this article can be found online at https://doi.org/10.1016/j.jelechem.2025.119653.

References

[1] E. Emanuele, A. Li Bassi, A. Macrelli, L. Magagnin, B. Bozzini, Enhancing secondary alkaline battery performance: synthesis and electrochemical characterization of Zn anodes, based on ZnO@C Core-Shell nanoparticles, ChemElectroChem 11 (13) (2024 Jul 2).
[2] B. Bozzini, C. Mele, A. Veneziano, N. Sodini, G. Lanzafame, A. Taurino, et al., Morphological evolution of Zn-sponge electrodes monitored by in situ X-ray computed microtomography, ACS Appl Energy Mater 3 (5) (2020 May 26) 4931–4940.
[3] J.F. Parker, I.R. Pala, C.N. Chervin, J.W. Long, D.R. Rolison, Minimizing shape change at Zn sponge anodes in rechargeable Ni–Zn cells: impact of electrolyte formulation, J. Electrochem. Soc. 163 (3) (2016) A351–A355.
[4] W. Long, Z. Yang, X. Fan, B. Yang, Z. Zhao, J. Jing, The effects of carbon coating on the electrochemical performances of ZnO in Ni-Zn secondary batteries, Electrochim. Acta 105 (2013) 40–46.
[5] J. Li, T. Zhao, E. Shangguan, Y. Li, L. Li, D. Wang, et al., Enhancing the rate and cycling performance of spherical ZnO anode material for advanced zinc-nickel secondary batteries by combined in-situ doping and coating with carbon, Electrochim. Acta 10 (236) (2017 May) 180–189.
[6] Z. Feng, Z. Yang, J. Huang, X. Xie, Z. Zhang, The superior cycling performance of the hydrothermal synthesized carbon-coated ZnO as anode material for zinc-nickel secondary cells, J. Power Sources 15 (276) (2015 Feb) 162–169.
[7] L. Li, S. Cheng, L. Deng, T. Liu, W. Dong, Y. Liu, et al., Effective solution toward the issues of Zn-based anodes for advanced alkaline Ni-Zn batteries, ACS Appl. Mater. Interfaces 15 (3) (2023 Jan 25) 3953–3960.
[8] D. Stock, S. Dongmo, J. Janek, D. Schröder, Benchmarking anode concepts: the future of electrically rechargeable zinc-air batteries, ACS Energy Lett. 4 (6) (2019 Jun 14) 1287–1300.
[9] J.F. Parker, J.S. Ko, D.R. Rolison, J.W. Long, Translating Materials-Level Performance into Device-Relevant Metrics for Zinc-Based Batteries vol. 2, Joule. Cell Press, 2018, pp. 2519–2527.
[10] Y. Wu, Y. Zhang, Y. Ma, J.D. Howe, H. Yang, P. Chen, et al., Ion-sieving carbon Nanoshells for deeply rechargeable Zn-based aqueous batteries, Adv Energy Mater. 8 (36) (2018 Dec 27).
[11] P. Chen, Y. Wu, Y. Zhang, T.H. Wu, Y. Ma, C. Pelkowski, et al., A deeply rechargeable zinc anode with pomegranate-inspired nanostructure for high-energy aqueous batteries, J. Mater Chem A Mater. 6 (44) (2018) 21933–21940.
[12] Y. Yan, Y. Zhang, Y. Wu, Z. Wang, A. Mathur, H. Yang, et al., A lasagna-inspired nanoscale ZnO anode design for high-energy rechargeable aqueous batteries, ACS Appl Energy Mater 1 (11) (2018 Nov 26) 6345–6351.
[13] D.E. Turney, J.W. Gallaway, G.G. Yadav, R. Ramirez, M. Nyce, S. Banerjee, et al., Rechargeable zinc alkaline anodes for Long-cycle energy storage, Chem. Mater. 29 (11) (2017 Jun 13) 4819–4832.
[14] Y.G. Zhu, T.M. Narayanan, M. Tulodziecki, H. Sanchez-Casalongue, Q.C. Horn, L. Meda, et al., High-energy and high-power Zn-Ni flow batteries with semi-solid electrodes, Sustain. Energy Fuels. 4 (8) (2020 Aug 1) 4076–4085.
[15] W. Mei, H. Chen, J. Sun, Q. Wang, The effect of electrode design parameters on battery performance and optimization of electrode thickness based on the electrochemical-thermal coupling model, Sustain. Energy Fuels. 3 (1) (2019) 148–165.
[16] M. Zhou, X. Zhou, Y. Yang, H. Yin, Y. Lei, S. Liang, et al., Issues and optimization strategies of binders for aqueous zinc metal batteries, Chem. Eng. J. Elsevier B.V. 497 (2024).
[17] D. Bresser, D. Buchholz, A. Moretti, A. Varzi, S. Passerini, Alternative binders for sustainable electrochemical energy storage-the transition to aqueous electrode processing and bio-derived polymers, Energ. Environ. Sci. 11 (11) (2018 Nov 1) 3096–3127.
[18] X. Han, L. Chen, M. Yanilmaz, X. Lu, K. Yang, K. Hu, et al., From nature, requite to nature: bio-based cellulose and its derivatives for construction of green zinc batteries, Chem. Eng. J. Elsevier B.V. 454 (2023).
[19] C.W. Lee, K. Sathiyanarayanan, S.W. Eom, H.S. Kim, M.S. Yun, Effect of additives on the electrochemical behaviour of zinc anodes for zinc/air fuel cells, J. Power Sources 160 (1) (2006 Sep 29) 161–164.
[20] S. Mu, È. Ller, F. Holzer, O. Haas, Optimized zinc electrode for the rechargeable zinc±air battery, 2025.
[21] C. Yang, Z. Zhang, Z. Tian, Y. Lai, K. Zhang, J. Li, Influences of carboxymethyl cellulose on two anodized-layer structures of zinc in alkaline solution, J. Alloys Compd. 15 (734) (2018 Feb) 152–162.
[22] S. Mu, È. Ller, F. Holzer, O. Haas, Optimized zinc electrode for the rechargeable zinc±air battery, 2025.
[23] B. Bozzini, A. Alleva, E. Emanuele, S. Gul, T. Qin, W. Yun, et al., Scale-up of zinc-air battery electrodes enhanced by 3D X-ray imaging, e-J. Nondestructive Testing [Internet] 30 (2) (2025 Feb). Available from: https://www.ndt.net/search/docs.php3?id=30736.
[24] B. Bozzini, M. Boniardi, T. Caielli, A. Casaroli, E. Emanuele, L. Mancini, et al., Electrochemical cycling behaviour and shape changes of Zn electrodes in mildly acidic aqueous electrolytes containing quaternary ammonium salts, ChemElectroChem 10 (12) (2023 Jun 14).
[25] P. Cloetens, M. Pateyron-Salomé, J.Y. Buffiere, G. Peix, J. Baruchel, F. Peyrin, M. Schlenker, Observation of microstructure and damage in materials by phase sensitive radiography and tomography, J. Appl. Phys. 81 (1997) 5878–5886.
[26] E. Emanuele, A.G. Agrios, A. Alleva, V. Bonanni, R. Ciancio, A. Gianoncelli, et al., Carbon-cloth supported ZnO Nanorods as binder-free zinc-ion battery anodes: an investigation into the electrode formation process, Adv Sustain Syst. 9 (6) (2025 Jun 1).
[27] H. Zhang, R. Wang, D. Lin, Y. Zeng, X. Lu, Ni-based nanostructures as high-performance cathodes for rechargeable Ni−Zn battery, ChemNanoMat 4 (6) (2018 Jun 1) 525–536.
[28] Lai S. Bin, M.I. Jamesh, X.C. Wu, Y.L. Dong, J.H. Wang, M. Gao, et al., A Promising Energy Storage System: Rechargeable Ni–Zn Battery vol. 36, Rare Metals. University of Science and Technology Beijing, 2017, pp. 381–396.
[29] S. Guo, L. Qin, J. Wu, Z. Liu, Y. Huang, Y. Xie, et al., Conversion-type anode chemistry with interfacial compatibility toward ah-level near-neutral high-voltage zinc ion batteries, Natl. Sci. Rev. 11 (7) (2024 Jul 1).
[30] Y.X. Song, Z.Y. Zhong, M.J. Chen, Y.Q. Ding, M. Zhou, Z.X. Liu, et al., Interfacial optimization enabling reversible and stable aqueous zinc metal batteries under harsh conditions, J. Cent. South Univ. 31 (12) (2024 Dec 1) 4536–4548.